Journal of Applied Physics

RESEARCH ARTICLE | MARCH 29 2023

Resonance, Rayleigh flows, and thermal choking: Compressible coolant states in porous electromagnetic heat exchangers

Ajit A. Mohekar; Burt S. Tilley ✉ ; Vadim V. Yakovlev

Journal of Applied Physics 133, 124906 (2023)
https://doi.org/10.1063/5.0139723

AIP Publishing

Journal of Applied Physics ARTICLE scitation.org/journal/jap

Resonance, Rayleigh flows, and thermal choking: Compressible coolant states in porous electromagnetic heat exchangers

Cite as: J. Appl. Phys. **133**, 124906 (2023); doi: 10.1063/5.0139723
Submitted: 22 December 2022 · Accepted: 11 March 2023 ·
Published Online: 29 March 2023

Ajit A. Mohekar,[1] Burt S. Tilley,[1,2,a)] and Vadim V. Yakovlev[2]

AFFILIATIONS

[1]Department of Mechanical Engineering, Worcester Polytechnic Institute, Worcester, Massachusetts 01609, USA
[2]Center for Industrial Mathematics and Statistics, Department of Mathematical Sciences, Worcester Polytechnic Institute, Worcester, Massachusetts 01609, USA

[a)]**Author to whom correspondence should be addressed:** tilley@wpi.edu

ABSTRACT

Electromagnetic (EM) heat exchangers (HX) are systems that convert EM energy into heat or mechanical work. One potential design consists of a porous lossy ceramic material heated by EM waves with a compressible gas coolant. EM heating of ceramics is nonlinear, since the loss factor is temperature dependent. Designing such EM HXs requires an understanding of coupling between temperature, the electric field, and gas dynamics at the pore scale. To mimic this microscale phenomenon, a single channel with a high-speed gas coolant in perfect thermal contact with a thin solid ceramic layer is considered, with an applied plane-wave electric field propagating normal to the channel walls. From a thin-domain asymptotic analysis, the conservation laws reduce to a Rayleigh flow in the gas coupled with averaged thermal energy conservation equations at leading order. The model predicts that the kinetic energy of the gas increases up to 12.5 times the inlet value when thermal runaway occurs in the ceramic region for the cases considered, and thermal choking is possible when the coolant reaches the sonic state. Local maxima of efficiency occur on a discrete set of ceramic thicknesses that correspond to Fabry–Bragg resonances of the electric field.

I. INTRODUCTION

Electromagnetic (EM) heating has been used for decades in thermal food applications,[1] chemical processes,[2] materials processing,[3] and a range of industrial heating applications.[4] The characteristic of this energy transfer is the conversion of EM energy into internal energy within the desired material. A phenomenon that occurs in this context is *thermal runaway*. In many EM lossy ceramic materials, such as zirconia or silicon carbide, the loss factor of the material increases with increasing temperature. At sufficiently high temperatures and sufficiently large applied electric field strengths, the average temperature in the medium can increase uncontrollably.[5] While this phenomenon may lead to significant destruction of the absorbing material, where this power able to be transferred at a sufficiently high rate to a coolant, a potentially large source of energy with a minimum increase in marginal applied power would be beneficial in a variety of applications.

The motivation for this work is the viability of utilizing thermal runaway in an electromagnetic heat exchanger (EM HX) where a ceramic absorber converts electromagnetic radiation to internal energy, and then this internal energy is transferred to a coolant. These devices are being considered in energy collection applications[6] and possibly a way to harness beamed energy.[7–10] A similar approach has been considered in beamed energy propulsion applications,[7] where NASA implemented a millimeter wave thermal launch system (MTLS) experiment.[11] An array of ceramic tubes is heated by high-power EM waves,[11] through which a high-pressure gas flows. The energy absorbed from EM waves provides a heat flux to this gas, which undergoes thermal expansion and provides thrust. For ground-to-ground power beaming applications, we are interested in understanding how much mechanical power can be generated at the outlet since the compressible gas dynamics is coupled with nonlinear EM heating of ceramic.

Distinctive in EM HX is that the rate of thermal absorption depends nonlinearly on the rate of energy transfer from the material, either through thermal losses or through the energy converted for useful work. Unlike classical resistive heating applications for heat exchangers, where the power source is independent of temperature and heat fluxes (e.g., Rostami *et al.*[12]), the electric field strength and the absorbed power are coupled nonlinearly to temperature in EM HXs: the electric field amplitude and temperature need to be solved simultaneously. Furthermore, steady-state temperatures that are predicted for these systems depend critically on the wavelength of the applied field and the geometry of the ceramic absorber.

For example, consider one-dimensional solutions of this coupled system for a lossy ceramic slab, infinite in extent and whose loss factor increases with increasing temperature. Kriegsmann[13] found that there are two stable thermal states when the slab thickness is much smaller than the wavelength of the applied electric field. For small applied electric field strengths, the absorbed energy in the ceramic balances energy losses from the slab via advection and radiation, and the resulting average slab temperature remains moderate. As the applied electric field strength is increased, however, a critical temperature is reached where energy losses to the environment are not sufficient to balance the absorbed power, and thermal runaway takes place. The second stable state results when the average slab temperature is large, on the order of 1800 K, such that the loss factor of the ceramic is significant. In this situation, the applied field is completely absorbed in a thin layer in the ceramic near the slab-air interface (i.e., the skin effect), and this absorbed power is balanced by radiation and convective losses to the environment. The transition between these two steady states is represented by a hysteresis diagram in the average temperature/applied external power plane, where the transition from the high-temperature state to the low temperature state occurs at lower applied electric field strengths compared to the transition from the low-temperature state to the high-temperature state. Extensions to these studies are found in multi-layer systems.[14–16]

More recently, we have been considering a third stable thermal state in multilayered slab systems. Consider three slabs of finite uniform thicknesses but infinite in extent, which are symmetrically irradiated by plane waves of equal electric field amplitude. The exterior slabs are lossless and have the same thickness, while the loss factor of the central ceramic increases with increasing temperature.[17–20] For appropriate choices of the slab thicknesses relative to the applied wavelength of the electric field and when the permittivity of exterior slabs is larger than the permittivity of the ceramic, a Fabry–Bragg resonance occurs within the ceramic. The loss factor results in a bounded electric field amplitude, and the resulting absorbed power in the ceramic is dissipated through either radiation or advection from the exterior of the external slabs. This phenomenon is also found in a grounded two laminate lossless-lossy system.[21] The average temperature of this state is intermediate to two equivalent states from the single-slab case: for materials like silicon carbide or zirconia, the average temperature is on the order of 1000 K, well below any temperature where structural material changes take place. While this intermediate solution branch is not pertinent to the situation we report here, the Fabry–Bragg resonance conditions do play a role in the energy absorption and transfer between the ceramic and the dielectric gaseous coolant.

This resonance condition has been utilized in other beamed energy contexts. In the NASA MTLS experiment,[11] an array of ceramic tubes is heated with an incident high-power beam of EM waves to realize the viability of beamed energy propulsion. When the ceramic tubes reach a sufficiently high temperature, a high-pressure compressed gas is expanded through tubes. Heat transfer from the energy absorbed by the ceramic tubes into the gas results in thermal expansion and provides the thrust of propulsion. The authors report that the maximum absorbed power by the ceramic tubes takes place when the tube thickness is one-quarter of the wavelength of the applied electric field: exactly the first mode of the Fabry–Bragg resonance.[11]

One potential design for an EM HX is inspired by the beamed propulsion experiment of Beach *et al.*[7] and to use an lossy porous medium through which the gaseous coolant flows and expands thermally as EM waves are applied. As a first effective model, the ceramic tube configuration in the NASA MTLS experiment can be represented as an ideal porous media, which obeys the capillary tubes model of porosity and permeability.[22] Generally, porous heat exchangers allow for a larger contact area between the fluid and the heated matrix, allowing better heat exchange between them. However, a viable EM HX design requires the understanding on coupling between the compressible gas dynamics and EM heating of the ceramic region at the pore scale. Buoyancy effects can be ignored at this scale since the characteristic Rayleigh number is negligible. However, thermal runaway is a phenomenon that is expected to occur.[20] Our goal in this work is to quantify the impact of coupling between thermal runaway and work of expansion taking place at the pore scale.

For this quantification, we focus on dominant physical processes to better understand the changes in energy and momentum transfer. We consider the case when the coolant Reynolds number is large, and inertia in the coolant flow is much larger than the effects of viscous stresses. The geometry of an idealized single pore of the EM HX is shown in Fig. 1. We exclusively consider gaseous coolants, as the temperatures post-thermal runaway (greater than 1000 K) make any known coolant remaining in the liquid phase highly unlikely. We assume that the coolant gas enters the channel with a known temperature, pressure, density, and flow velocity such that gas is subsonic at the inlet. Through conduction from the EM-heated ceramic, the gas undergoes thermal expansion and accelerates as it moves from the inlet to the outlet. The resultant increase in kinetic energy of the coolant at the output provides a measure by which the efficiency of the energy conversion can be quantified.

An outline of this paper is as follows. In Sec. II, we formulate the mathematical problem in dimensionless form. In Sec. III, we consider the thin domain limit, where the thicknesses of the channel and ceramic are much smaller than their lengths. In Sec. IV, we show that the compressible coolant problem follows a Rayleigh flow and identify the connection between fluid inertia and temperature. In Sec. V, we discuss the computational results of our model and explore the connections between EM heating and the increase in the fluid kinetic energy. We conclude in Sec. VI.

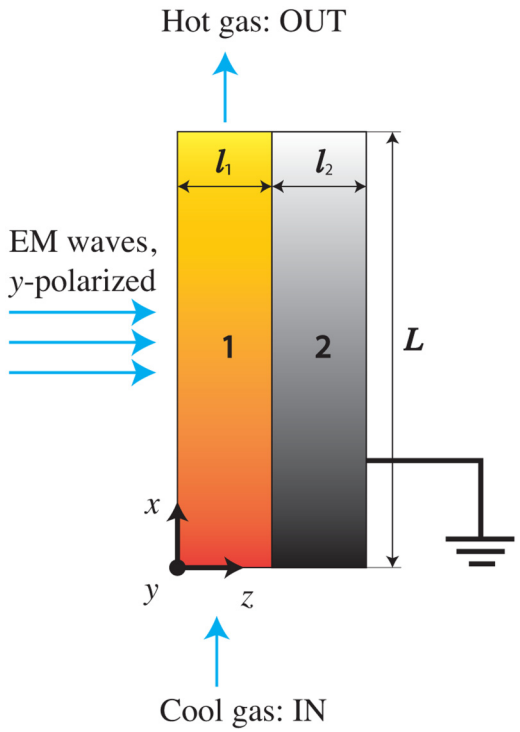

FIG. 1. Structure of the considered EM HX. Region 1 is a pressure-driven flow of an ideal gas and region 2 is a lossy ceramic material.

II. PROBLEM FORMULATION

Consider an idealized two-layer EM HX of length L, as shown in Fig. 1. In the left layer, labeled region 1 in Fig. 1 is a channel through which a gaseous coolant flows from bottom to top. In the right layer, labeled region 2 is a lossy dielectric material, such as silicon carbide or zirconia, whose right surface is electrically grounded. The layer thicknesses l_1 and l_2 are assumed to be much smaller than length L. Plane EM waves, polarized in the y-direction, propagate normally to the structure. Only the ceramic is heated by EM waves, and the fluid is heated through perfect thermal contact with the ceramic at $z = l_1$. As is common in EM heating models, the period of the carrier wave is much shorter than the characteristic time scales of either thermal advection or thermal diffusion, and so we assume the electric field is harmonic on these transport time scales (e.g., see Kriegsmann[13]). Furthermore, we focus here only on steady-state solutions.

The steady mass and momentum equations for the gas in region 1 ($0 < x < L$, $0 < z < l_1$) are given by Euler's equations,[23]

$$\nabla \cdot (\rho\, \mathbf{u}) = 0, \tag{1}$$

$$\mathbf{u} \cdot \nabla \mathbf{u} = -\frac{1}{\rho_1} \nabla p, \tag{2}$$

where $\mathbf{u} = (u(x, z), w(x, z))$ is the gas velocity, $\rho_1(x, z)$ is the gas mass density, and $p(x, z)$ is the gas gauge pressure, as referenced from the ambient atmospheric pressure P_A. We assume an ideal gas and include thermal diffusion within the gas to arrive at the equations[23] in region 1,

$$P_A + p(x, z) = \rho_1(x, z)\, R_g\, T_1(x, z), \tag{3}$$

$$\rho_1\, c_{v,1} \{\mathbf{u} \cdot \nabla T_1\} + (P_A + p)\, \nabla \cdot \mathbf{u} = \kappa_1 \nabla^2\, T_1, \tag{4}$$

where R_g is the universal gas constant per unit mass, $T_1(x, z)$ is the temperature of the coolant, $c_{v,1}$ is the specific heat of the gas at constant volume, and κ_1 is the thermal conductivity within the gas. In region 2, thermal diffusion and Joule heating from the applied electric field are the two energy transport mechanisms,[24]

$$\kappa_2\, \nabla^2 T_2 + \frac{1}{2}\, \sigma_{eff} |\mathbf{E}_2|^2 = 0, \tag{5}$$

where κ_2 is the thermal conductivity in region 2, $T_2(x, z)$ is the temperature in the ceramic, and σ_{eff} is the effective electrical conductivity in the ceramic. We assume that there is no free charge within the ceramic and that the effective conductivity depends only on the frequency of the electromagnetic wave, ω, and its temperature-dependent loss factor $\epsilon_{i,2}(T_2(x, z))$, [24]

$$\sigma_{eff} = \epsilon_o\, \omega\, \epsilon_{i,2}(T_2), \tag{6}$$

where $\omega = 2\pi f$, f is the frequency of EM radiation and ϵ_o is the permittivity of the free space.

Finally, we note that in both regions there is an electric field present. We assume a monochromatic wave that is being applied, and this gives us the following Gauss and Helmholtz equations[25] in each region j,

$$\nabla \cdot (\tilde{\epsilon}_j\, \mathbf{E}_j) = 0, \tag{7}$$

$$\nabla^2 \mathbf{E}_j + \tilde{k}_j^2 \mathbf{E}_j = \nabla(\nabla \cdot \mathbf{E}), \tag{8}$$

where $\mathbf{E}_j$ is the electric field in region j, $\tilde{\epsilon}_j = \epsilon_o\, \epsilon_j = \epsilon_o(\epsilon_{r,j} + i\, \epsilon_{i,j})$ is the electrical permittivity in each region j, $i = \sqrt{-1}$, and ϵ_o is the free-space permittivity. Since the gas is assumed to be lossless, $\epsilon_{i,1} = 0$, we assume that relative dielectric constants $\epsilon_{r,j} \geq 1$ are real. The wavenumber in each layer is given by $\tilde{k}_j = \omega\sqrt{\mu_o \tilde{\epsilon}_j}$, where μ_o is the magnetic permeability in free space and the permeability of both gas and the ceramic. The wavenumber in the ceramic $\tilde{k}_2$ is temperature dependent and complex-valued.

We assume that the applied electric field for $z \to -\infty$, polarized in the y-direction, is given by

$$\mathbf{E} \sim E_o \left\{ e^{i \tilde{k}_o z} + \Gamma\, e^{-i \tilde{k}_o z} \right\} \mathbf{j} + c.c., \tag{9}$$

where E_o is the electric field amplitude, $\tilde{k}_o = \omega\sqrt{\mu_o\, \epsilon_o}$ is the free-space wave number, Γ is the reflection coefficient, $\mathbf{j}$ is the unit vector in the y-direction, and $c.c.$ is an abbreviation for the

complex conjugate of the previous term. This assumption for the applied electric field gives the following vector formulation for the electric field in each region $j = 1, 2$,

$$\mathbf{E}_j = E_o\, E_j(x, z)\, \mathbf{j} + c.c., \tag{10}$$

where $E_j(x, z)$ is the complex-valued electric field amplitude in region j. Note that this plane-wave form gives that both $\nabla \cdot \mathbf{E}_j = 0$ and $\nabla \cdot \{\tilde{\boldsymbol{\epsilon}}_j \mathbf{E}_j\} = 0$ for all (x, z), and $j = 1, 2$.

The boundary conditions for the velocity and temperature at $z = 0$ are no normal mass flux of the gas, and the normal heat flux is balanced by Newton's law of cooling and radiation losses, respectively,[26]

$$w = 0, \tag{11}$$

$$\kappa_1 \frac{\partial T_1}{\partial z} = h\{T_1 - T_A\} + \xi\, s_r \left[T_1^4 - T_A^4\right], \tag{12}$$

where h is the heat transfer coefficient, $T_A = P_A/(\rho_A R_g)$ is the ambient temperature in the environment with ρ_A being the ambient coolant density, ξ is the radiation emissivity of the surface, and s_r is the Stefan–Boltzmann radiation constant. Furthermore, at $z = 0$, the electric and magnetic fields need to be continuous, and this leads to the following boundary condition at $z = 0$,[13]

$$\frac{\partial E_1}{\partial z} + i\tilde{k}_o E_1 = 2\, i\tilde{k}_o E_o. \tag{13}$$

Along the right channel wall at $z = l_1$, we require no gas mass flux through the boundary, perfect thermal contact between the coolant and the ceramic,[26] and continuity of the electric and magnetic fields,[25]

$$w = 0, \tag{14}$$

$$T_1 = T_2, \tag{15}$$

$$\kappa_1 \frac{\partial T_1}{\partial z} = \kappa_2 \frac{\partial T_2}{\partial z}, \tag{16}$$

$$E_1 = E_2, \tag{17}$$

$$\frac{\partial E_1}{\partial z} = \frac{\partial E_2}{\partial z}. \tag{18}$$

For $z = l_1 + l_2$, we assume that this boundary is thermally insulated and grounded,

$$\frac{\partial T_2}{\partial z} = 0, \tag{19}$$

$$E_2 = 0. \tag{20}$$

At the coolant inlet $x = 0$, we assume that the x-component of the velocity is uniform in z and the z-component of the velocity is zero, and that the coolant is under ambient conditions,

$$\underline{x = 0}: (u, w) = (U_{in}, 0), \tag{21}$$

$$T_1 = T_A, \tag{22}$$

$$p = 0, \tag{23}$$

$$\rho = \rho_A. \tag{24}$$

To better understand the dominant physical effects, we perform a nondimensional analysis so that each nondimensional parameter is a ratio of two physical quantities with the same physical units. We scale z on l_1, x on L, u on U_{in}, w on $l_1\, U_{in}/L$, ρ_1 on ρ_A, p on $\rho_A\, U_{in}^2$, T_j on T_A, and the variables $x, z, u, w, p, T_j, \rho_1, E_j$ to derive the dimensionless variables with these scales. A result of this process gives a set of dimensionless groups that can be interpreted as ratios of two physical processes with same units. By applying the dimensional values of our system listed in Table I, the dimensionless groups allow us to then efficiently identify the dominant physical effects within a given scenario. Cases where some of these parameters are either very large or very small allow for reduced models to be formulated in this limits through the perturbation analysis.[28]

The dimensional versions of conservation of mass (1) and conservation of momentum (2) become on the dimensionless spatial region $0 < x < 1$, $0 < z < 1$,

$$\frac{\partial}{\partial x}\{\rho_1 u\} + \frac{\partial}{\partial z}\{\rho_1 w\} = 0, \tag{25}$$

TABLE I. Dimensional parameters used in the model. Properties of air (region 1) are taken from Bergman *et al.*[26] and zirconia (region 2) properties are taken from Yakovlev *et al.*.[27]

Parameters	Values
R_g	287 J/kgK
ρ_A	1.16 kg/m^3
T_A	300 K
c_{v_1}	713 J/kgK
κ_1	0.02 W/mK
γ	1.4
l_1	0.01 m
U_{in}	60 m/s
c_{p_2}	210 J/kgK
κ_2	0.2 W/mK
ϵ_o	8.85×10^{-12} F/m
f	2.45 GHz
$\epsilon_{i,2}$	$0.00293e^{2.32\left(\frac{T-T_A}{T_A}\right)}$
$\epsilon_{r,1}$	1
$\epsilon_{r,2}$	6.69
μ_0	$4\pi \times 10^{-7}$ H/m
l_2	0.01 m
L	1 m

$$\rho_1\left\{u\frac{\partial u}{\partial x}+w\frac{\partial u}{\partial z}\right\}+\frac{\partial p}{\partial x}=0, \tag{26}$$

$$\eta^2\rho_1\left\{u\frac{\partial w}{\partial x}+w\frac{\partial w}{\partial z}\right\}+\frac{\partial p}{\partial z}=0, \tag{27}$$

where $\eta = l_1/L$ is the aspect ratio of the channel. In addition, the equation of state (3), conservation of energy (4), and the Helmholtz Eq. (8) for region 1 become

$$\rho_1=\frac{1}{T_1}\left(1+M^2\,p\right), \tag{28}$$

$$\eta\,Pe\left\{\rho_1\left(u\frac{\partial T_1}{\partial x}+w\frac{\partial T_1}{\partial z}\right)+(\gamma-1)\left(1+M^2\,p\right)\left[\frac{\partial u}{\partial x}+\frac{\partial w}{\partial z}\right]\right\} =\frac{\partial^2 T_1}{\partial z^2}+\eta^2\frac{\partial^2 T_1}{\partial x^2}, \tag{29}$$

$$\frac{\partial^2 E_1}{\partial z^2}+k_1^2\,E_1+\eta^2\frac{\partial^2 E_1}{\partial x^2}=0, \tag{30}$$

where $Pe = (l_1\,U_{in}\rho_A\,c_{v,1})/\kappa_1$ is the Péclet number, the ratio of convective heat transport to conduction, and the ratio of the flow velocity to the speed of sound is given by $M^2 = U_{in}^2/(R_g\,T_A)$ or the Mach number, γ is the ratio of the specific heat of the gas, and $k_1 = \tilde{k}_1\,l_1$ is the dimensionless wave number of the electric field in the coolant, or the ratio of the channel width to the wavelength of the electric field.

In the ceramic, the scaled versions of conservation of energy (5) and the Helmholtz equation (8) on the domain $0 < x < 1$, $1 < z < 1 + l$ are given by

$$\frac{\partial^2 T_2}{\partial z^2}+\eta^2\frac{\partial^2 T_2}{\partial x^2}+\eta P\,\epsilon_{i,2}(T_2)|E_2|^2=0, \tag{31}$$

$$\frac{\partial^2 E_2}{\partial z^2}+k_2^2\,E_2+\eta^2\frac{\partial^2 E_2}{\partial x^2}=0, \tag{32}$$

where $l = l_2/l_1$ is the ratio of the thickness of the ceramic to the channel thickness and $P = (\epsilon_o\,\omega\,l_1\,L\,E_o^2)/(2\,T_A\,\kappa_2)$ is the ratio of the applied power density to the surface compared to the characteristic conductive heat flux.

At the boundary between free-space and the gas, $z = 0$, we require that the normal gas flow is zero (11), the heat flux from the gas is balanced by advection and radiation to the environment (12), and that the electric and magnetic fields are continuous (13) at the boundary,

$$w=0, \tag{33}$$

$$\frac{\partial T_1}{\partial z}=\eta\left\{Bi\,(T_1-1)+R\left(T_1^4-1\right)\right\}, \tag{34}$$

$$\frac{\partial E_1}{\partial z}+i\,k_o\,E_1=2\,i\,k_o, \tag{35}$$

where $Bi = h\,L/\kappa_1$ is the Biot number or the ratio of convective heat transport to the surroundings to the conductive heat transfer in the coolant. The radiation number $R = \xi\,s_r\,L\,T_A^3/\kappa_1$ is the ratio of characteristic radiation losses to the environment to conduction within the coolant, and $k_o = \tilde{k}_o\,l_1$ is the scaled free-space wavenumber.

At the boundary between the gas and the ceramic, $z = 1$, we require that the normal gas flow is zero (14), perfect thermal contact between the gas and the ceramic (15)–(16), and continuity between electric and magnetic fields in the gas and the ceramic (17)–(18) become

$$w=0, \tag{36}$$

$$T_1=T_2, \tag{37}$$

$$\frac{\partial T_1}{\partial z}=\kappa\frac{\partial T_2}{\partial z}, \tag{38}$$

$$E_1=E_2, \tag{39}$$

$$\frac{\partial E_1}{\partial z}=\frac{\partial E_2}{\partial z}, \tag{40}$$

where $\kappa = \kappa_2/\kappa_1$ is the ratio of the thermal conductivities of the ceramic and the gaseous coolant.

At the thermally insulated (19) and grounded (20) boundary of the ceramic $z = 1 + l$, we have

$$\frac{\partial T_2}{\partial z}=0, \tag{41}$$

$$E_2=0. \tag{42}$$

Finally, we note that, at the inlet $x = 0$, we have $u(0, z) = 1$, $w(0, z) = 0$, $\rho_1(0, z) = 1$, $p(0, z) = 0$, and $T_1(0, z) = 1$.

III. THIN-DOMAIN LIMIT

To better understand coupling of the physical phenomena of this problem, we look at the asymptotic limit $\eta \ll 1$. We expand all unknown variables in asymptotic series in terms of η,

$$\rho_1=\rho_1^{(0)}+\eta\rho_1^{(1)}+\cdots, \tag{43}$$

$$p=p^{(0)}+\eta p^{(1)}+\cdots, \tag{44}$$

$$u=u^{(0)}+\eta u^{(1)}+\cdots, \tag{45}$$

$$w=w^{(0)}+\eta w^{(1)}+\cdots, \tag{46}$$

$$E_1 = E_1^{(0)} + \eta E_1^{(1)} + \cdots, \tag{47}$$

$$E_2 = T_2^{(0)} + \eta E_2^{(1)} + \cdots, \tag{48}$$

$$T_1 = T_1^{(0)} + \eta T_1^{(1)} + \cdots, \tag{49}$$

$$T_2 = T_2^{(0)} + \eta T_2^{(1)} + \cdots. \tag{50}$$

Substituting (43)–(50) into the dimensionless system of Eqs. (25)–(30), we find at leading order for the gas equations,

$$\frac{\partial}{\partial x}\left\{\rho_1^{(0)} u^{(0)}\right\} + \frac{\partial}{\partial z}\left\{\rho_1^{(0)} w^{(0)}\right\} = 0, \tag{51}$$

$$\rho_1^{(0)}\left\{u^{(0)}\frac{\partial u^{(0)}}{\partial x} + w^{(0)}\frac{\partial u^{(0)}}{\partial z}\right\} + \frac{\partial p^{(0)}}{\partial x} = 0, \tag{52}$$

$$\frac{\partial p^{(0)}}{\partial z} = 0, \tag{53}$$

$$\rho_1^{(0)} = \frac{1}{T_1^{(0)}}\left(1 + M^2 p^{(0)}\right), \tag{54}$$

$$\frac{\partial^2 T_1^{(0)}}{\partial z^2} = 0, \tag{55}$$

$$\frac{\partial^2 E_1^{(0)}}{\partial z^2} + k_1^2 E_1^{(0)} = 0, \tag{56}$$

and in the ceramic,

$$\frac{\partial^2 T_2^{(0)}}{\partial z^2} = 0, \tag{57}$$

$$\frac{\partial^2 E_2^{(0)}}{\partial z^2} + k_2^2 E_2^{(0)} = 0, \tag{58}$$

along with the following boundary conditions,

$$\underline{z = 0}: \quad w^{(0)} = 0, \tag{59}$$

$$\frac{\partial T_1^{(0)}}{\partial z} = 0, \tag{60}$$

$$\frac{\partial E_1^{(0)}}{\partial z} + i\,k_o E_1^{(0)} = 2\,i\,k_o, \tag{61}$$

$$\underline{z = 1}: \quad w^{(0)} = 0, \tag{62}$$

$$T_1^{(0)} = T_2^{(0)}, \tag{63}$$

$$\frac{\partial T_1^{(0)}}{\partial z} = \kappa \frac{\partial T_2^{(0)}}{\partial z}, \tag{64}$$

$$E_1^{(0)} = E_2^{(0)}, \tag{65}$$

$$\frac{\partial E_1^{(0)}}{\partial z} = \frac{\partial E_2^{(0)}}{\partial z}, \tag{66}$$

$$\underline{z = 1 + l}: \quad \frac{\partial T_2^{(0)}}{\partial z} = 0, \tag{67}$$

$$E_2^{(0)} = 0. \tag{68}$$

From (53), we see that $p^{(0)}(x, z) = p(x)$ is independent of the spanwise coordinate z, and from (55) and (60) that $T_1^{(0)}(x, z) = T_1^{(0)}(x)$ is also independent of z. So from the equation of state (54), $\rho_1^{(0)}(x, z) = \rho(x)$ is also z-independent. Similarly from (57) and (67) that $T_2^{(0)}(x, z) = T_2^{(0)}(x)$. So from perfect thermal contact at $z = 1$, Eq. (64) gives us that $T_1^{(0)}(x) = T_2^{(0)}(x) = T(x)$.

For the flow field, we assume a plug flow $u^{(0)}(x, z) = u(x)$, $w^{(0)} = 0$, which after one integral of mass conservation (25) in x, we find that

$$\rho(x)\,u(x) = m, \tag{69}$$

where m is the uniform mass flow rate of the gas coolant. Using the inlet boundary condition at $x = 0$, we find that $m = 1$, but we keep the notation in the following derivation. Finally, we have the classical Bernoulli relation and the equation of state,

$$\rho(x)\,u(x)\,\frac{du}{dx} + \frac{dp}{dx} = m\,\frac{du}{dx} + \frac{dp}{dx} = 0, \tag{70}$$

$$\rho(x) = \frac{1}{T(x)}\left\{1 + M^2 p(x)\right\}. \tag{71}$$

.

The temperature being independent of z also simplifies the leading-order Helmholtz problems in the gas and the ceramic to be, where we drop the (0) superscript and consider this the leading-order problem to solve in terms of unknown temperature $T(x)$,

$$\frac{\partial^2 E_1}{\partial z^2} + k_1^2 E_1 = 0,\ 0 < z < 1, \tag{72}$$

$$\frac{\partial^2 E_2}{\partial z^2} + k_2^2(T(x))E_2 = 0,\ 1 < z < 1 + l, \tag{73}$$

subject to boundary conditions,

$$\frac{\partial E_1}{\partial z}(x, 0) + i\,k_o E_1(x, 0) = 2\,i\,k_o, \tag{74}$$

$$E_1(x, 1) = E_2(x, 1), \tag{75}$$

$$\frac{\partial E_1}{\partial z}(x,\,1) = \frac{\partial E_2}{\partial z}(x,\,1), \tag{76}$$

$$E_2(x,\,1+l) = 0. \tag{77}$$

We still need to find an expression for $T(x)$ in order to close our leading-order problem. To do this, we look at the energy equations (29) and (31) using (43)–(50) at $O(\eta)$,

$$\frac{\partial^2 T_1^{(1)}}{\partial z^2} = Pe\left\{m\frac{dT}{dx} + (\gamma-1)(1+M^2p(x))\frac{du}{dx}\right\}, \tag{78}$$

$$\kappa\,\frac{\partial^2 T_2^{(1)}}{\partial z^2} = -\kappa\,P\epsilon_{i,2}(T(x))|E_2|^2, \tag{79}$$

where we have formally multiplied (79) intentionally by κ as is clarified below. Equations (78) and (79) are subject to boundary conditions in z,

$$\frac{\partial T_1^{(1)}}{\partial z}(x,\,0) = Bi\,(T(x)-1) + R\,(T^4(x)-1), \tag{80}$$

$$T_1^{(1)}(x,\,1) = T_2^{(1)}(x,\,1), \tag{81}$$

$$\frac{\partial T_1^{(1)}}{\partial z}(x,\,1) = \kappa\frac{\partial T_2^{(1)}}{\partial z}(x,\,1), \tag{82}$$

$$\frac{\partial T_2^{(1)}}{\partial z}(x,\,1+l) = 0. \tag{83}$$

For the compatibility condition on $T(x)$ in order for the solutions to exist, we integrate both sides of (78) over $0<z<1$ and add the result to the integral of (79) over $1<z<1+l$. The net result using (80)–(83) gives the required condition on $T(x)$,

$$Pe\left\{m\frac{dT}{dx} + (\gamma-1)(1+M^2\,p(x))\frac{du}{dx}\right\} = P\,\epsilon_{i,2}(T(x))||E_2||^2 - Bi\,(T(x)-1) - R(T^4(x)-1), \tag{84}$$

where

$$||E_2||^2 = \int_1^{1+l} |E_2(x,\,z)|^2\,dz. \tag{85}$$

Finally, we are interested in the large velocity limit, $Pe \gg 1$, and so we define the $O(1)$ quantities $\bar{P} = P/Pe$, $\bar{Bi} = Bi/Pe$, and $\bar{R} = R/Pe$ to arrive at the final system of equations,

$$\rho(x)\,u(x) = m,\;\; 0<x<1, \tag{86}$$

$$m\frac{du}{dx} + \frac{dp}{dx} = 0,\;\; 0<x<1, \tag{87}$$

$$m\frac{dT}{dx} + (\gamma-1)(1+M^2\,p(x))\frac{du}{dx} = Q(T(x)),\;\; 0<x<1, \tag{88}$$

$$\rho(x) = \frac{1}{T(x)}\left(1+M^2p(x)\right),\;\; 0<x<1, \tag{89}$$

$$Q(T(x)) = \kappa\bar{P}\epsilon_{i,2}(T(x))||E_2||^2 - \bar{Bi}(T(x)-1) - \bar{R}\left(T^4(x)-1\right), \tag{90}$$

$$\frac{\partial^2 E_1}{\partial z^2} + k_1^2 E_1 = 0,\;\; 0<z<1, \tag{91}$$

$$\frac{\partial^2 E_2}{\partial z^2} + k_2^2(T(x))E_2 = 0,\;\; 1<z<1+1, \tag{92}$$

subject to boundary conditions,

$$\underline{x=0}\colon\; u=\rho=T=1,\, p=0, \tag{93}$$

$$\underline{z=0}\colon\; \frac{\partial E_1}{\partial z} + i\,k_o E_1 = 2\,i\,k_o, \tag{94}$$

$$\underline{z=1}\colon\; E_1 = E_2, \tag{95}$$

$$\frac{\partial E_1}{\partial z} = \frac{\partial E_2}{\partial z}, \tag{96}$$

$$\underline{z=1+l}\colon\; E_2 = 0. \tag{97}$$

IV. RAYLEIGH FLOW

The systems (86)–(89) represent a spatially varying plug flow through a channel into which an energy flux Q enters this system. We briefly outline the development of the *Rayleigh flow* in this section and discuss later how this flow couples with the electromagnetic problem (91)–(97).

From (86) and (89), we can write

$$u = \frac{mT}{1+M^2p}. \tag{98}$$

Taking the x-derivative of (98) and utilizing the momentum equation (87), we get

$$\left(1-\frac{M^2u^2}{T}\right)\frac{du}{dx} = \left(\frac{u}{T}\right)\frac{dT}{dx}. \tag{99}$$

We define the *dynamic Mach number* $\bar{M}^2$ as

$$\bar{M}^2 = \frac{M^2\,u^2}{\gamma\,T}. \tag{100}$$

Substituting (100) in the above Eq. (99), we get

$$(1-\gamma\bar{M}^2)\frac{du}{dx}=\frac{u}{T}\frac{dT}{dx}. \tag{101}$$

Substituting (98) and (101) into energy conservation Eq. (88) results in

$$m\frac{dT}{dx}=Q(T)\left[\frac{1-\gamma\bar{M}^2}{\gamma(1-\bar{M}^2)}\right]. \tag{102}$$

Substituting (102) into (101), we get

$$\frac{du}{dx}=\left[\frac{uQ(T)}{mT}\right]\left[\frac{1}{\left(1-\gamma\bar{M}^2\right)}\right]\left[\frac{1-\gamma\bar{M}^2}{\gamma(1-\bar{M}^2)}\right]. \tag{103}$$

We can solve the system of nonlinear first-order ODEs (102) and (103) for given inlet conditions on temperature and flow velocities (93).

However, we can follow Babu[29] and find a relation between $\bar{M}$ and T in terms of their inlet conditions $\bar{M}_o$ and T_o. From (102) and (103), we can write following differential identities:

$$\frac{dT}{T}=\frac{Q(T)}{mT}\left[\frac{1-\gamma\bar{M}^2}{\gamma(1-\bar{M}^2)}\right]dx, \tag{104a}$$

$$\frac{du}{u}=\left[\frac{1}{\left(1-\gamma\bar{M}^2\right)}\right]\frac{dT}{T}. \tag{104b}$$

Taking the differential of both sides of (100), we find

$$\frac{d(\bar{M}^2)}{\bar{M}^2}=2\frac{du}{u}-\frac{dT}{T}. \tag{105}$$

Substituting (104) into (105), we get

$$\frac{d(\bar{M}^2)}{\bar{M}^2}=\left[\frac{1+\gamma\bar{M}^2}{1-\gamma\bar{M}^2}\right]\frac{dT}{T}. \tag{106}$$

Equation (106) exactly describes the classical Rayleigh flow. To simplify even further, we can separate variables and integrate both sides of (106) from inlet to outlet conditions. Upon integration, we find

$$\frac{T}{T_0}=\left(\frac{\bar{M}^2}{\bar{M}_0^2}\right)\left(\frac{1+\gamma\bar{M}^2}{1+\gamma\bar{M}_0^2}\right)^{-2}, \tag{107}$$

where T_0 is the inlet temperature and $\bar{M}_0^2$ is the dynamic Mach number at the inlet that is given as $\bar{M}_0^2=\frac{M^2}{\gamma T_0}$ (as $u=1$ at the inlet). For given inlet conditions T_o and $\bar{M}_o^2$, the system of differential Eqs. (102) and (107) can be solved numerically.

Before we discuss results from this model, let us first look at the algebraic constrain (107) separately to get some insights into the numerical solution to the full problem. As Eq. (107) is quadratic in nature, for a given $\frac{T}{T_0}$, there are two possible solutions for the Mach number. These two roots are given by

$$\bar{M}_1^2=\frac{-b-\sqrt{b^2-4ac}}{2a},\ \bar{M}_2^2=\frac{-b+\sqrt{b^2-4ac}}{2a}, \tag{108}$$

where $a=\gamma^2$, $b=2\gamma-\frac{T_0}{\bar{M}_0^2T}(1+\gamma\bar{M}_0^2)^2$, and $c=1$.

Roots of the algebraic constraint (107) are plotted in Fig. 2 assuming that the inlet Mach number is such that the flow is subsonic with $\bar{M}_0=0.0298$ based on values listed in Table I For this inlet condition, the following observations can be made from (108) and (102):

- When the heat added into the system is due to EM heating of the ceramic, i.e., when $Q(T)>0$, the right hand side of (102) is positive for $\bar{M}_0^2<\frac{1}{\gamma}$. The outlet temperature monotonically increases with the applied EM power, $\bar{P}$. This situation corresponds to stage I as shown in Fig. 2, and we see that the outlet $\bar{M}^2$ also increases with both T and $\bar{P}$.

(1) Regardless of the applied EM ower, the maximum temperature that can be achieved in the system is $T=T_{\max}$, which occurs when $\bar{M}^2=\frac{1}{\gamma}$ as seen in Fig. 2. By taking the derivative of (107) with respect to $\bar{M}^2$ and setting the result to zero, the maximum temperature, $T_{\max}$, is given by

$$T_{\max}=\frac{T_0(1+\gamma\bar{M}_0^2)^2}{4\gamma\bar{M}_0^2}, \tag{109}$$

and the corresponding gain in the kinetic energy per unit

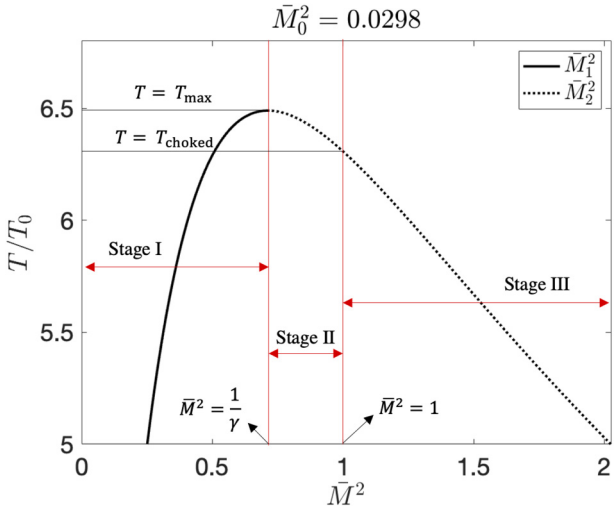

FIG. 2. Two roots of the algebraic constraint given by (108) as a function of $\frac{T}{T_0}$ for $\bar{M}_0^2=0.0298$, i.e., inlet velocity and temperatures are $u_{\text{in}}=60$ m/s and 300 K, respectively.

volume, $\frac{1}{2}\rho u^2$, is given by

$$\frac{\rho_{out}u_{out}^2}{\rho_{in}u_{in}^2} = m\,u_{max} = m\left(\frac{T_{\max}}{\gamma \bar{M}_o^2}\right)^{1/2} \approx 12.5, \qquad (110)$$

based on the values given in Table I.

- With some algebraic manipulations on (102) and (106), it is possible to show that

$$m\frac{d(\bar{M}^2)}{dx} = \bar{M}^2\left[\frac{1+\gamma\bar{M}^2}{\gamma(1-\bar{M}^2)}\right]\frac{Q(T)}{T}. \qquad (111)$$

The right-hand side of this equation is always positive when $\bar{M}^2 < 1$. We can then conclude that if the flow is subsonic at the inlet, $Q(x) > 1$ results in an elevated Mach number at the outlet up to $\bar{M}^2 = 1$ (i.e., the model allows for $\bar{M}^2$ at the outlet monotonically increases with $\bar{P}$ until we reach $\bar{M}^2 = 1$).

- When $\bar{P}$ is such that $Q(T) > 0$ and $\frac{1}{\gamma} < \bar{M}^2 < 1$ within a computational domain defined as $x_{\text{crit}} < x < 1$, the right-hand side of (102) is negative for $x > x_{\text{crit}}$. This means that the gas experiences cooling effect for $x > x_{\text{crit}}$ as a result of additional heat within the ceramic. The relation between $\bar{M}^2$ and T for this scenario is described by stage II in Fig. 2.
- When $\bar{P}$ is increased even further and $Q(T)$ is such that $\bar{M}^2 = 1$ within the computational domain, the RHS of (102) becomes $-\infty$, and further increase in $\bar{M}^2$ is not possible. This phenomenon is known as *thermal choking* in classical Rayleigh flows. Theoretically, it means that when the flow is initially subsonic, no matter how much heat we add into the system, it is not possible to reach a supersonic state (i.e., $\bar{M}^2 > 1$) at the outlet. Experimentally, if we keep adding heat into the system even further, the outlet $\bar{M}^2$ suggests that the flow remains in the sonic state , but the inlet properties, such as gas temperature or pressure, change to accommodate further additional heat. The model presented here does not consider the impact of heat addition into an thermal choked flow (this is the limit on Rayleigh flow approximation). In the Results section below, we consider cases when thermal choking is absent. We discuss this phenomenon in more detail in upcoming subsections.

V. RESULTS

We now solve the system (102) and (107) computationally using for inlet conditions $\bar{M}_o^2 = 0.0298$ [corresponding to the gas inlet velocity of 60 m/s, $T_o = 1$ (corresponding to 300 K)], $\bar{Bi} = 0.4$, and $\bar{R} = 0.1$. Based on our scaling, $m = 1$ as well. The model is solved using the package *ode15s* function within MATLAB[30–32] and validated through convergence tests on the relative tolerance, for a case where thermal runaway takes place. Furthermore, results from a second-order adaptive midpoint rule script on the first-order differential Eq. (111) provided a check on the accuracy of our approach. Figure 3 shows this comparison between the two models when thermal runaway takes place in the ceramic.

Results from this model are organized as follows:

- We first explain the thermal energy balance taking place in the EM HX when we operate in stage I shown in Fig. 2, i.e., at the outlet, we have $\bar{M}^2 \leq \frac{1}{\gamma}$ and $T \leq T_{\max}$. In this stage I, it is expected that both T and $\bar{M}^2$ at the outlet increase monotonically with $\bar{P}$.
- We then consider the operation of the EM HX in stage II shown in Fig. 2, i.e., at the outlet, we have $\frac{1}{\gamma} < \bar{M}^2_{\text{outlet}} < 1$ and T_{outlet} that drops with an increase in $\bar{P}$ (also $T_{\text{outlet}} < T_{\max}$). By carrying out a linear stability analysis, we show that stage II is unstable such that infinitesimal fluctuations in the applied EM power lead to rapid rise in $\bar{M}^2$, resulting in a thermally choked flow.
- Finally, we explain thermal choking phenomenon and discuss possible approaches to avoid choking experimentally.

1. Operation in stage I

Results from the solution to (102) and (106) for $\bar{P} = 10$ and $\bar{P} = 50$ are plotted in Fig. 4. When $\bar{P} = 10$, we operate on the lower branch of the response curve (as seen from the temperature

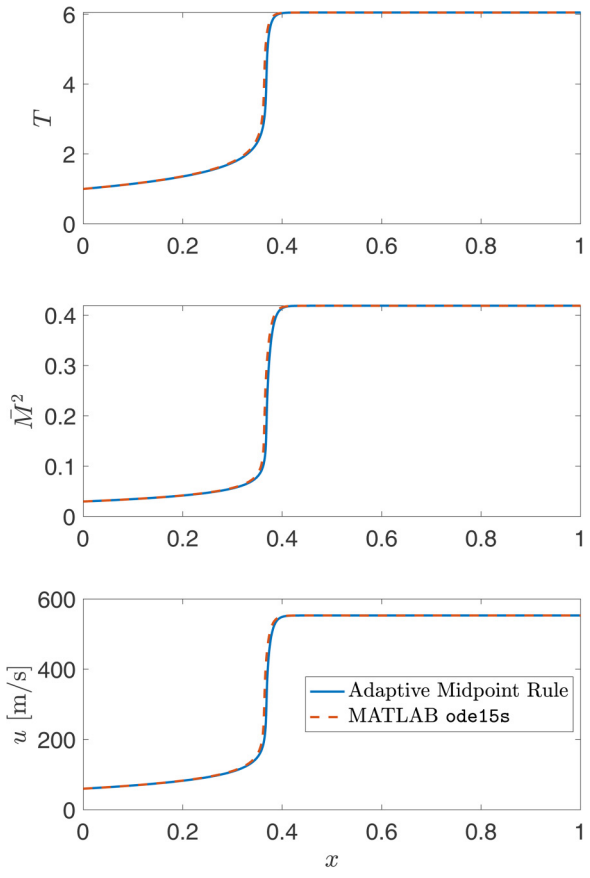

FIG. 3. Comparison between solutions obtained using MATLAB ode15s function [which solves (102) and (107)] and the adaptive midpoint rule [which solves (111) and and (107)] when $\bar{P} = 50$. Mean errors between the models are 0.97%, 1.4%, and 1.2% for comparison of T, $\bar{M}^2$, and u solutions, respectively. $\bar{P} = 50$, $\bar{Bi} = 0.4$, *and* $\bar{R} = 0.1$.

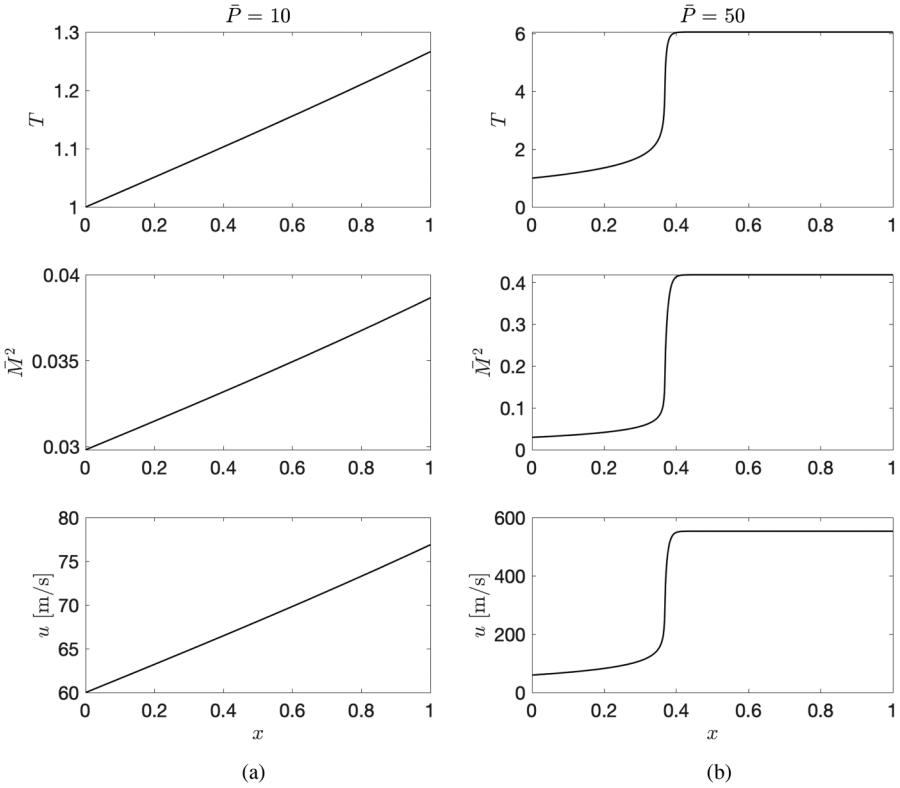

FIG. 4. Results from the solution to (102) and (106) when $\bar{P} = 10$ (a) and $\bar{P} = 50$ (b). Common parameters in these models are $\bar{Bi} = 0.4$, $\bar{R} = 0.1$, and inlet velocity and temperature are $u_{\text{in}} = 60\,\text{m/s}$ and $T_{\text{in}} = 1$, respectively.

values), and the kinetic energy (KE) of the gas per unit volume at the outlet, i.e., $\text{KE} = \frac{1}{2}\rho u^2$, turns out to be 1.5 times the KE at the inlet. However, when $\bar{P} = 50$, we observe the onset of thermal runaway in the ceramic region as seen from the jump in temperature values. As a result, we observe a jump in KE about nine times the initial value.

For this scenario, the competition between thermal runaway and the skin effect can be seen from Fig. 5. When the EM heat source is large, the onset of thermal runaway takes place, but as a result of increased $\epsilon_{i,2}$, we observe the skin effect, i.e., most of the incident EM energy is absorbed at the interface between the fluid channel and the ceramic. Since there is less EM power available for heating, q_{dot} drops down and is balanced by net heat losses to the environment, i.e., $Q(T) = 0$. Since heat is not being added into the ceramic, both T and u become uniform in space until the outlet at $x = 1$. The power response equation that gives us $Q(T) = 0$ can be written as

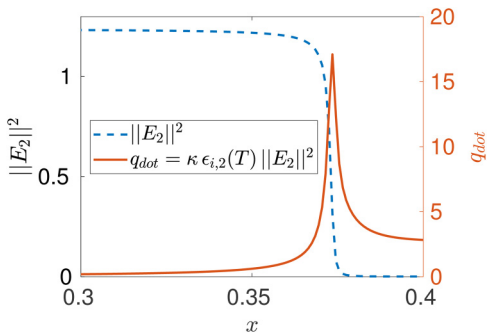

FIG. 5. Normalized electric field strength, $\|E_2\|^2$, and $q_{\text{dot}} = \kappa\|E_2\|^2\epsilon_{i,2}(T)$ as a function of x in the region where thermal runway takes place when $\bar{P} = 50$. Values are normalized by dividing the respective local maximum. Temperature profile for this scenario is shown in Fig. 4(b).

$$\bar{P} = \frac{\bar{Bi}(T-1) + \bar{R}(T^4-1)}{\kappa\|E_2(T)\|^2\epsilon_{i,2}(T)}. \tag{112}$$

In Fig. 6, we plot the outlet temperature as a function of $\bar{P}$ given by the numerical model of (102) and (107) and the analytical solution to Eq. (112). As expected, both the models agree with each other as the skin effect causes $Q(T) = 0$. When thermal runway initiates within the ceramic, the phenomenon of the skin effect promotes the balance between the EM heat source and environmental heat losses. This balance stabilizes the temperature growth, and the energy balance is then given by (112) [i.e., $Q(T) = 0$]. But, when we operate on the lower branch, the temperature monotonically increases over the domain $0 < x < 1$, as seen from Fig. 4(a). A large spatial domain is needed for the computed temperature to arrive at the value described in the lower branch of the analytical

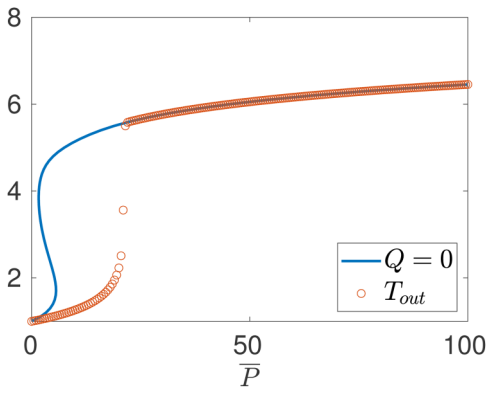

FIG. 6. Comparison of power response curves given by the numerical solution to (102) and (107) and analytical solution to (112). The model of (112) assumes that the temperature is uniform in space.

solution. This distinction in the domain length explains why the response curves do not agree on the lower branch.

From this comparison shown in Fig. 6, we show that the outlet conditions (T_{outlet} and $\bar{M}^2_{\text{outlet}}$) in stage I can be determined by simultaneously solving two nonlinear Eqs. (112) and (101). This simplification is valid only when thermal runaway takes place in the ceramic, and the EM HX is operated on the upper branch of the response curve. Until otherwise noted, we will use this simplification to determine the outlet conditions of the EM HX when operated in stage I.

2. Operation in stage II and thermal choking

We now set $\bar{P}$ such that we have $\bar{M}^2_{\text{outlet}} > \frac{1}{\gamma}$ at the outlet (i.e., the EM HX operates in the stage II shown in Fig. 2) when $\bar{M}^2_0 = 0.0298$ (i.e., inlet velocity of 60 m/s), $T_0 = 1$, $\bar{B}i = 0.4$ and $\bar{R} = 0.1$. Results from the numerical model are shown in Fig. 7. As seen in Figs. 7(a) and 7(b), the gas experiences a cooling effect when $\bar{M}^2 > \frac{1}{\gamma}$ [as the RHS of (102) becomes negative for $\bar{M}^2 > \frac{1}{\gamma}$] and $\bar{M}^2$ monotonically increases with $\bar{P}$ [as the RHS of (111) is always positive for $\bar{M}^2 < 1$]. In Fig. 7(c), we plot $\bar{M}^2_{\text{outlet}}$ as a function of $\bar{P}$ when the EM HX operates in stages I and II. We see that the increase in $\bar{M}^2$ with $\bar{P}$ is very sharp in stage II in comparison to stage I (i.e., $\bar{M}^2$ is very sensitive to the applied power in stage II). To understand why this occurs, we carry out a linear stability analysis on uniform and constant solutions at steady-state (i.e., outlet conditions when thermal runway occurs). We define T_{ss} and $\bar{M}^2_{\text{ss}}$ as uniform base-state solutions that satisfy the algebraic constraint (107). Now introducing infinitesimal perturbations in the base-state solution as

$$T = T_{\text{ss}} + \tilde{T},$$
$$\bar{M}^2 = \bar{M}^2_{\text{ss}} + \tilde{\bar{M}}^2,$$

and linearizing (102) and (107) about the uniform base-state solution, we get

$$m\gamma\left(1 - \bar{M}^2_{\text{ss}}\right)\frac{d\tilde{T}}{dx} = \left[m\gamma\frac{dT_{\text{ss}}}{dx} - Q(T_{\text{ss}})\gamma\right]\tilde{\bar{M}}^2 + \left[(1 - \gamma\bar{M}^2_{\text{ss}})\left(\frac{dQ}{dT}\right)_{T_{\text{ss}}}\right]\tilde{T}, \tag{113a}$$

$$\tilde{T} = \left[\left(\frac{1 + \gamma\bar{M}^2_0}{1 + \gamma\bar{M}^2_{\text{ss}}}\right)^2 - \frac{2\gamma T_{\text{ss}}}{1 + \gamma\bar{M}^2_{\text{ss}}}\right]\tilde{\bar{M}}^2. \tag{113b}$$

We can further simplify the linearized system of Eq. (113) by utilizing that we have $\frac{dT_{\text{ss}}}{dx} = 0$ and $Q(T_{\text{ss}}) = 0$ (this is true when thermal runaway occurs in the ceramic). Finally, we assume that $\tilde{T} = Ae^{sx}$, where A and s are amplitude and growth rate of infinitesimal perturbations. Substituting $\tilde{T}$ in (113) and solving for s, we get

$$s = \frac{(1 - \gamma\bar{M}^2_{\text{ss}})\left(\frac{dQ}{dT}\right)_{T_{\text{ss}}}}{m\gamma(1 - \bar{M}^2)},$$

where $\left(\frac{dQ}{dT}\right) = k\bar{P}\left[\frac{d(\|E_2\|^2)}{dT}\epsilon_{1,2}(T) + \|E_2\|^2\frac{d\epsilon_{1,2}}{dT}\right] - \bar{B}i - 4\bar{R}T^3$. As the uniform base-state solution is assumed to be on the upper branch, we can look at Fig. 5 and conclude that $\frac{d(\|E_2\|^2)}{dT} < 0$ and $\|E_2\|^2 \to 0$ and $\left(\frac{dQ}{dT}\right)_{T_{\text{ss}}} < 0$ on the upper branch near the outlet (this observation is consistent with Refs. 13, 17, and[18]). We can then conclude that when $\bar{M}^2_{\text{ss}} < \frac{1}{\gamma}$, s is negative, which means that the outlet solution is linearly stable against infinitesimal perturbations. However, when $\bar{M}^2_{\text{ss}} > \frac{1}{\gamma}$, s becomes positive. This means that infinitesimal disturbances introduced in the temperature solution at the outlet are growing exponentially in space. As a result of this instability, $\bar{M}^2$ increases rapidly until it reaches 1 (i.e., sonic state), and we achieve thermal choking within the channel.

The Rayleigh flow becomes thermally choked when $\bar{M}^2 = 1$. The linear stability analysis above shows that stage II is very sensitive to disturbances in the applied power (i.e., disturbances in T and $\bar{M}^2$). For instance, if we let $\bar{P}_{\text{choked}} = \bar{P}_{\text{crit}} + \Delta\bar{P}$, where $\bar{P}_{\text{crit}}$ and $\bar{P}_{\text{choked}}$ are the applied powers, when $\bar{M}^2_{\text{outlet}} = \frac{1}{\gamma}$ and $\bar{M}^2_{\text{outlet}} = 1$, respectively. From Fig. 7(c), we get $\Delta\bar{P} = 0.02$ for $\bar{M}^2_0 = 0.0298$, $T_0 = 1$, $\bar{B}i = 0.4$, and $\bar{R} = 0.1$. When this instability is promoted, small changes in the applied power lead to rapid growth of T and $\bar{M}^2$ leading to a thermally choked flow. Although operating an EM HX in stage II suggests generation of maximum possible KE of the gas, these states may not be possible without the thermally choked channel flow.

In many aerospace application, such as aircraft engines or external combustion engines, heat is added into a subsonic flow of a gas to achieve the desired gas velocity. We show that the gain in the gas flow velocity is proportional to how much heat is being added into the gas by the engine. But, theoretically, when the flow reaches the sonic state, further additional heat is not possible without altering the inlet condition due to thermal choking. Experimentally, alternations in the inlet condition due to thermal

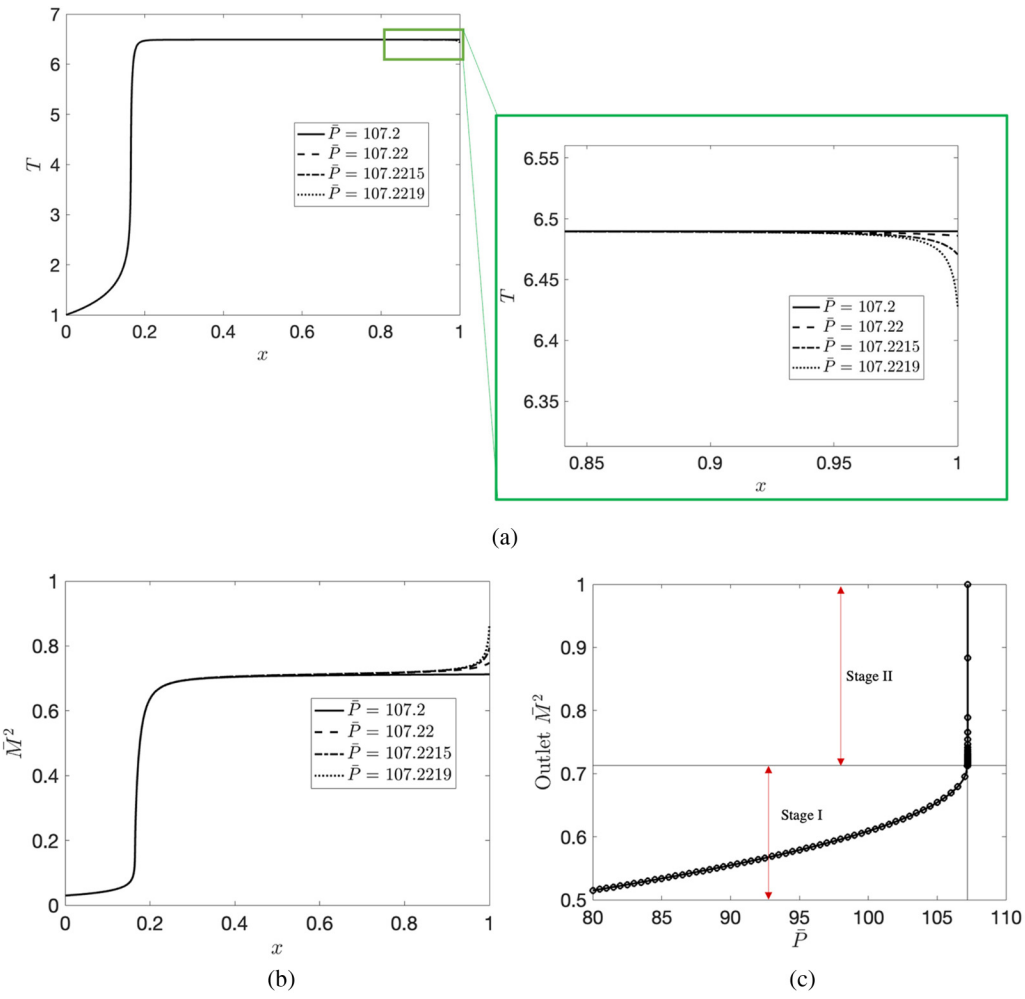

FIG. 7. Temperature profiles (a) and $\bar{M}^2$ (b) as a function x with increasing applied EM power, $\bar{P}$ when operated in stage II shown in Fig. 2. $\bar{M}^2_{\text{outlet}}$ as a function of $\bar{P}$ (c) when operated in stages I and II. Parameters that are kept constant in these simulations are $\bar{M}_0^2 = 0.0298$, $T_0 = 1$, $\bar{Bi} = 0.4$, and $\bar{R} = 0.1$.

choking lead to drop in mechanical power output of the engine.[33] If the heat is added into the flow that is supersonic at the inlet, shock waves can occur as a result of thermal choking, and again performance of the engine drops down.[29] Therefore, in typical aircraft engines, heat is added into a subsonic flow to achieve $\bar{M}^2 < 1$ and different types of nozzle assemblies are used to reach supersonic states at the outlet.

The EM HX discussed here is also limited by thermal choking. When $\bar{M}^2 = 1$, right-hand side of (102) becomes $-\infty$ indicating thermal choking, i.e., conservation laws can no longer be described by Rayleigh flow approximation.

To determine the critical power at which thermal choking occurs, we identify that stage II (which is defined when $\frac{1}{\gamma} < \bar{M}^2 < 1$) is unstable such that infinitesimal fluctuations in T or $\bar{M}^2$ make the flow to become thermally choked. However, when the EM HX is operated in stage I, we achieve a stable operation. The maximum possible $\bar{M}^2$ and T in stage I are $\bar{M}^2_{\max} = \frac{1}{\gamma}$ and $T_{\max}$ given by (109), respectively. If we let P_{crit} to be the applied EM power when at the outlet we have $\bar{M}^2_{\text{outlet}} = \frac{1}{\gamma}$ and $T_{\text{outlet}} = T_{\max}$, then thermal choking is absent when $\bar{P} < \bar{P}_{\text{crit}}$. Since this state lies in stage I, we can utilize simplification that the balance between thermal runaway and the skin effect results in $Q(T) = 0$ and the outlet conditions can be determined by simultaneously solving two nonlinear equations (112) and (107). Since our goal is to determine $\bar{P}_{\text{crit}}$ such that $T_{\text{out}} = T_{\max}$ and $\bar{M}^2_{\text{outlet}} = \frac{1}{\gamma}$, we can solve (112) for a given $T_{\max}$ as

$$\bar{P}_{\text{crit}} = \frac{\bar{Bi}(T_{\max} - 1) + \bar{R}(T_{\max}^4 - 1)}{\kappa \|E_2\|^2(T_{\max})\epsilon_{i,2}(T_{\max})}. \tag{114}$$

From (109), $T_{\max}$ increases nonlinearly as $\bar{M}_0^2$ decreases. This suggests that $\bar{P}_{\text{crit}}$ also increases as $\bar{M}_0^2$ decreases. We now solve (109)

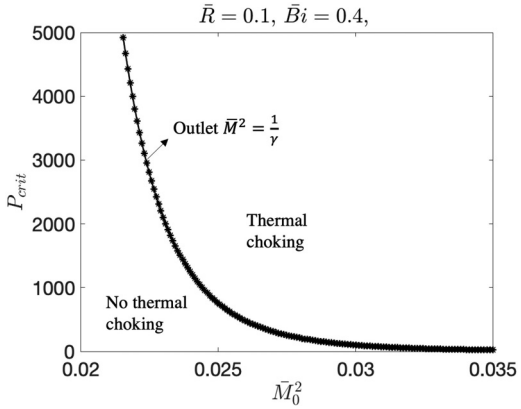

FIG. 8. Critical power, $\bar{P}_{\text{crit}}$, as a function of inlet Mach number $\bar{M}_0^2$. When $\bar{P} = \bar{P}_{\text{crit}}$, $\bar{M}^2_{\text{outlet}} = \frac{1}{\gamma}$ and $T_{\text{outlet}} = T_{\text{max}}$ as given by (109).

and (114) for different values of $\bar{M}_0^2$, and this result is plotted in Fig. 8. From this curve, it is possible to choose inlet flow speeds depending on the incident power levels such that thermal choking can be avoided, which we think is helpful for future EM HX design.

3. Power efficiency

One of the benefits of our approach is in finding an estimate of the efficiency for these heat exchangers as described by nondimensional groups. In this section, we focus on the characteristics of the system for which the heat transfer from the absorbed energy in the ceramic is converted to mechanical work in the gas. We choose this efficiency since we expect the energy loss to reflection of the electromagnetic energy to be significant. For example, Hogan *et al.*[10] through FDTD simulations consider the EM heating of families of AlN:Mo at different volume fractions of molybdenum. They report reflected losses of incident power in the range of 45%–70% at temperatures in the range of 1100 K. This then results in a total efficiency of EM heat generation to be in the range of 30%–55%.

To consider the power efficiency of the power that is not reflected from the system, we integrate the conservation of energy [Eq. (88)] in x from zero to one to arrive at the following balance of power terms, arranged so that each term is positive,

$$P_{therm} + P_{env} + P_{rad} = P_{abs} + P_{flow} = P_{total}, \tag{115}$$

where $P_{therm} = m\{T(1) - T(0)\}$ is the power needed to raise the temperature of the fluid. The additional energy loss terms on the

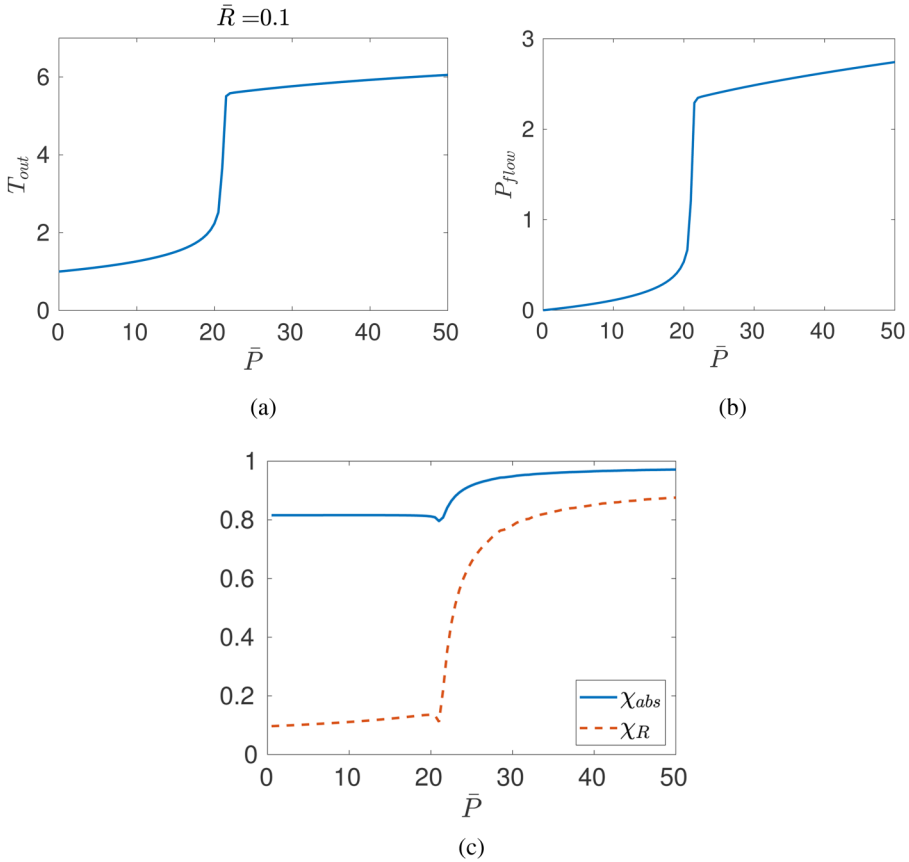

FIG. 9. (a) Outlet temperature T_{out} as a function of the dimensionless input power $\bar{P}$ for $\bar{R} = 0.1$, $\bar{Bi} = 0.4$, and $l = 1$. (b) Net output flow power P_{flow} as a function of $\bar{P}$. (c) Efficiency for absorbed power χ_{abs} compared to the efficiency of radiation losses χ_R. Note that after thermal runaway, the increase in absorbed power is mostly lost through radiation.

left-hand side of (115) are given by

$$P_{env} = \overline{Bi}\int_0^1 [T(x) - 1]\, dx, \tag{116}$$

$$P_{rad} = \overline{R}\int_0^1 \left[T^4(x) - 1\right] dx, \tag{117}$$

where P_{env} is the net power loss due to environmental losses and P_{rad} are the losses due to thermal radiation. The right-hand side consists of power absorbed by the ceramic, and the power converted to useful work due to thermal expansion,

$$P_{abs} = \kappa\bar{P}\int_0^1 \epsilon_{i,2}(T)\, \|E_2\|^2\, dx, \tag{118}$$

$$P_{flow} = (\gamma - 1)\left\{\frac{M^2}{2}\left[u^2(1) - 1\right] - (1 + M^2)[u(1) - 1]\right\}, \tag{119}$$

where we have assumed inlet conditions $u(0) = T(0) = 1$ and $p(0) = 0$.

In order to determine the conversion efficiency of the system, we use as a reference power P_{total} and consider what fraction of this power corresponds to terms on the left-hand side of (115), which we label as *losses*. The power fractions for terms on the right-hand side of (115) coincide with power efficiencies,

$$\chi_{thermal} = \frac{P_{thermal}}{P_{total}}, \tag{120}$$

$$\chi_{env} = \frac{P_{env}}{P_{total}}, \tag{121}$$

$$\chi_R = \frac{P_{rad}}{P_{total}}, \tag{122}$$

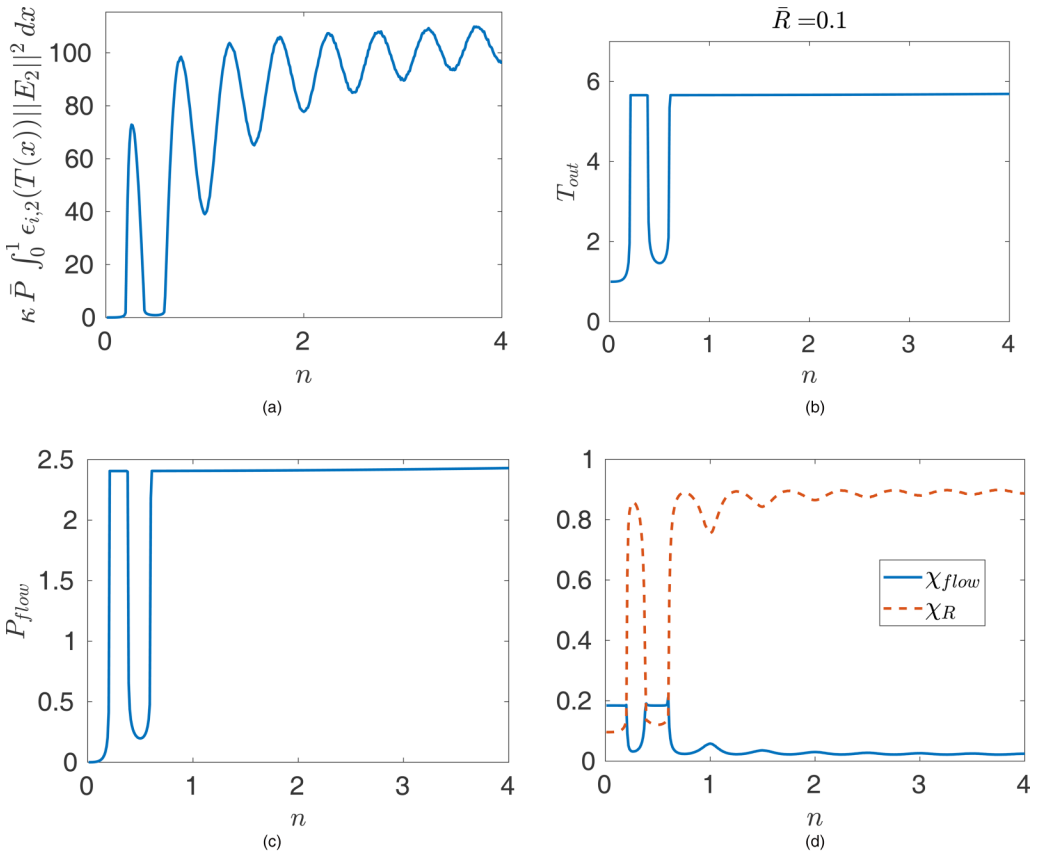

FIG. 10. Ceramic thickness effect on power with $\bar{P} = 20$, $\bar{R} = 0.1$, $\overline{Bi} = 0.4$, and $0 \le n \le 4$. (a) P_{abs} vs n; (b) T_{out} vs n; (c) P_{flow} vs n; and (d) power fractions χ_{flow} and χ_R vs n.

$$\chi_{abs} = \frac{P_{abs}}{P_{total}}, \tag{123}$$

$$\chi_{flow} = \frac{P_{flow}}{P_{total}}. \tag{124}$$

To better understand the interplay of these power fractions, we show a typical measure of these powers over $0 < \bar{P} < 30$ in Fig. 9, where $\bar{R} = 0.1$, $\overline{Bi} = 0.5$, and $l = 1$. In Fig. 9(a), we show the outlet temperature T_{out} as a function of $\bar{P}$ and note that the outlet temperature attains the value of the upper branch of the power response curve around $\bar{P} = 20$. Since $m = 1$ in our case, $T_{out} = P_{thermal} + 1$, and we see the corresponding behavior in the flow power P_{flow} in Fig. 9(b). However, the fraction of power given to increase the flow decreases significantly for $\bar{P} > 20$, as shown in Fig. 9(c). We note that while the absorbed power fraction P_{abs} increases from 0.8 to nearly 1 at $\bar{P} = 30$, the fraction of losses of the system to radiation significantly increase from near 0.1 for small $\bar{P}$ to over 0.8 for $\bar{P} = 30$. Hence, the increased energy absorption due to the onset of thermal runaway does increase the outlet flow power, but the majority of the power is lost through radiation effects.

The dimensionless wavelength of the electric field in the ceramic is given by

$$\lambda_2 = \frac{2\pi}{k_o \sqrt{\epsilon_{r,2}}}.$$

From Mohekar *et al.* (2020),[21] we note that our system has electromagnetic resonances at odd multiples of $\lambda_2/4$, and we then consider variations of the ceramic thickness in terms of the wavelength in the ceramic,

$$l = \lambda_2 n, \tag{125}$$

where the Fabry–Bragg resonance occurs for $n = 1/4, 3/4, 5/4, \ldots$.

In Fig. 10, we show the responses of these power contributions as a function of n for $\bar{P} = 20$ and the remainder of the parameters the same as in Fig. 9. In Fig. 10(a), we plot the absorbed power P_{abs} as a function of n and note that the maxima of the absorbed power occur exactly at Fabry-Bragg resonance conditions. However, the outlet temperature shown in Fig. 10(b) appears to reach its outlet temperature provided that the absorbed power P_{abs} is approximately

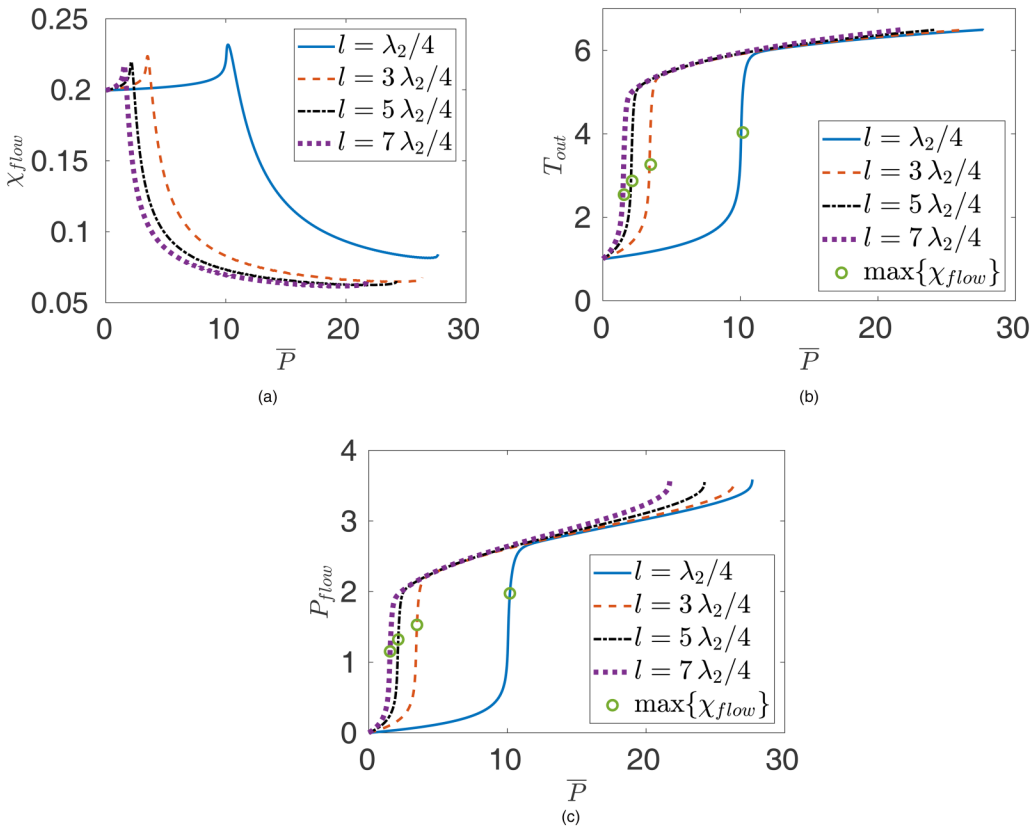

FIG. 11. Resonant frequency impact on $\bar{P}$-dependence for (a) χ_{flow}; (b) T_{out}; and (c) P_{flow}. Plots are terminated before $\bar{P} = 30$ are a result of thermal choking.

larger than 40. The flow power P_{flow} tracks with T_{out} as expected as shown in Fig. 10(c), but the fraction of the power needed to maintain this flow decreases with increasing n, and the losses are primarily due to radiation as shown in Fig. 10(d). From these results, it is clear that a significant increase in the output flow is possible near $n = 1/4$, and that this increase is amenable to values of n near this value. This is consistent with the NASA's MTLS experiment[11] where it is reported that the maximum absorption of the EM power occurs when the ceramic tube is 1/4 wavelength thick.

With this result, we can focus on the effects of the power response of the system over $\bar{P}$ for different resonance values. Figure 11a shows the flow power efficiency χ_{flow} as a function of $\bar{P}$ for the resonance cases $n = 1/4$, $3/4$, $5/4$, and $7/4$. Note that for each resonance case, the efficiency reaches a peak value before decaying algebraically as $\bar{P}$ increases. The value of $\bar{P}$ needed to achieve this peak-efficiency case decreases as n increases. However, from the outlet temperature T_{out} and net flow power P_{flow} shown in Figs. 11(b) and 11(c), we note that the outlet values at these peak efficiencies, shown by the open green circles, *decrease* with increasing n. This suggests that the power efficiency may not be the best metric in determining a system design:

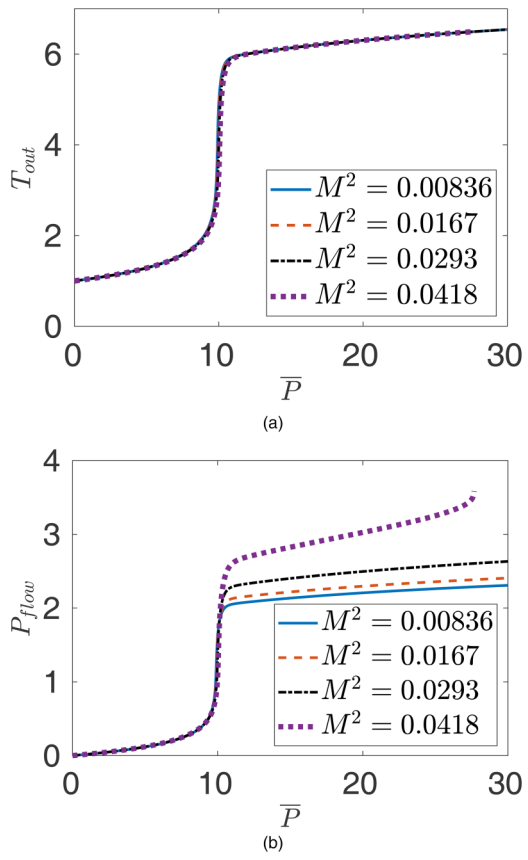

FIG. 12. $\bar{P}$-dependence of (a) T_{out} and (b) P_{flow} over M^2. Graphs that terminate before $\bar{P} = 30$ are cases where thermal choking takes place.

reduced efficiency may be the price to pay to gain an eightfold increase in the flow power.

A final note on Fig. 11(c) is that at nearly the same flow power $P_{flow} \approx 3.3$, the onset of thermal choking takes place. We consider here reducing the inlet flow velocity to prevent thermal choking and see how this change affects the output power. This is done by reducing the Mach number M^2. In Fig. 12(a), we show the outlet temperature T_{out} as a function of $\bar{P}$ for a range of M^2. The value $M^2 = 0.0418$ corresponds to our previous results, and we see that the change in the outlet temperature behavior over $\bar{P}$ for these Mach numbers is not significant. However, for the flow power P_{flow} shown in Fig. 12(b), we note that the output power values vary with M^2 appreciably for $\bar{P} > 10$. Thermal choking only takes place for $\bar{P} < 30$ for the cases described above.

VI. CONCLUSIONS

In this paper, we consider a simple two-layer model of an EM HX, where in one layer flows a gaseous coolant and the second layer consists of a lossy dielectric. This second layer is heated by an externally applied EM field. The gas flow dynamics, electromagnetics, and the energy transport are nonlinearly coupled and the mathematical system representing these processes need to be solved simultaneously. We look in the limit of large *Re* and order-one Mach numbers to gain physical insight into the behavior and potential of this EM HX.

By applying the thin domain asymptotic theory to governing equations, we derive a system of ODEs that governs the cross-sectional averaged conservation laws and electric field strength, which is then solved numerically in MATLAB. We have shown that when a plug flow is assumed in the channel, the leading-order system of equations is reduced to a typical *Rayleigh flow* coupled with EM heating of the ceramic. We consider the inlet conditions such that the flow is subsonic, but with heat entering the channel from the ceramic, the gas undergoes thermal expansion and accelerates as it moves from the inlet to outlet. We find that the kinetic energy of the gas is elevated by at most 12.5 times the initial value at the inlet when thermal runaway occurs in the ceramic for the cases which we considered.

The model of Rayleigh flow coupled with EM heating of ceramics is limited by the phenomenon of thermal choking. When flow velocity and temperatures are such that we reach sonic state ($\bar{M}^2 = 1$) within the channel, thermal choking occurs and the further addition of heat is not possible without altering the inlet flow conditions. By carrying out the linear stability analysis, we find that when we have $\frac{1}{\gamma} < \bar{M}^2 < 1$ inside the computational domain, infinitesimal fluctuations in temperatures (or the applied EM power) lead to a rapid rise in flow velocity, resulting in to a thermally choked flow. Through this stability analysis, we have determined the critical applied EM power, $\bar{P}_{\text{crit}}$ such that when $\bar{P} > \bar{P}_{\text{crit}}$, small fluctuations $\bar{P}$ lead to thermal choking in the channel. By carrying out a parametric study, we have then determined how this critical applied EM power is affected by the inlet flow conditions. This result is significant from the practical application point of view as it allows us to design experiments by avoiding thermal choking within the fluid region. The maximum practical Mach number that can be achieved is $\frac{1}{\gamma}$, and the expression

governing the maximum possible temperature within the channel has been derived.

To determine the effectiveness of the EM HX, total thermal and mechanical efficiencies of the device are calculated. It is found that the most efficient operation occurs when high temperatures are achieved at the low applied power when thermal runaway initiates. By carrying out parametric studies on l_2, we find that the electric field resonance occurs in the ceramic layer if $l_2 = \frac{n\lambda_2}{4}$, where n can be any odd integer. As a result, thermal runaway occurs at low applied powers when we increase the value of n, and this causes maximum efficiency of the energy conservation to increase with n. To further improve the effectiveness of the power generation from porous EM HX, future work can be focused on considering array of multiple long and thin structures considered here.

ACKNOWLEDGMENTS

The authors are grateful to the Air Force Office of Scientific Research, Award No. FA9550-18-1-0528, for their support of this work. Lively discussions with Drs. Brad Hoff and Zane Cohick at AFRL-Kirtland Air Force Base were much appreciated.

AUTHOR DECLARATIONS

Conflict of Interest

The authors have no conflicts to disclose.

Author Contributions

Ajit A. Mohekar: Conceptualization (equal); Formal analysis (equal); Methodology (lead); Software (equal); Writing – original draft (lead). **Burt S. Tilley:** Conceptualization (lead); Funding acquisition (lead); Project administration (lead); Supervision (lead); Writing – review & editing (equal). **Vadim V. Yakovlev:** Conceptualization (equal); Funding acquisition (supporting); Project administration (supporting); Supervision (supporting); Writing – review & editing (equal).

DATA AVAILABILITY

The data that support the findings of this study are available within the article.

REFERENCES

[1]A. K. Datta, *Handbook of Microwave Technology for Food Application* (Marcel Decker, Inc., 2001).
[2]N. E. Leadbeater, *Microwave Heating as a Tool for Sustainable Chemistry* (CRC Press, 2010).
[3]J. A. Aguilar-Garib, "Thermal microwave processing of materials," in *Advances in Induction and Microwave Heating of Mineral and Organic Materials*, edited by S. Grundas (Intech Open, Rijeka, Croatia, 2011), pp. 243–268.
[4]S. Chandrasekaran, S. Ramanathan, and T. Basak, "Microwave material processing—A review," AIChE J. **58**, 330–363 (2012).
[5]M. Chandran, V. Bogdan Neculaes, D. Brisco, S. Katz, J. Schoonover, and L. Cretegny, "Experimental and numerical studies of microwave power redistribution during thermal runaway," J. Appl. Phys. **114**, 204904 (2013).
[6]A. Jamar, Z. Majid, W. Azmi, M. Norhafana, and A. Razak, "A review of water heating system for solar energy applications," Int. Commun. Heat Mass Transfer **76**, 178–187 (2016).
[7]P. George and R. Beach, "Beamed-energy propulsion (BEP) study," Tech. Rep. (NASA, 2012), NASA/TM-2012-127014.
[8]P. Kumi, S. A. Martin, V. V. Yakovlev, M. S. Hilario, B. W. Hoff, and I. M. Rittersdorf, "Electromagnetic-thermal model of a millimeter-wave heat exchanger based on an AlN: Mo susceptor," COMPEL-Int. J. Comp. Math. Electr. Electron. Eng. **39**, 481–496 (2020).
[9]B. Hoff, M. Hilario, B. Jawdat, A. Baros, F. Dynys, J. Mackey, V. Yakovlev, C. Andraka, K. Armijo, E. Savrun, and I. Rittersdorf, "Millimeter wave interactions with high temperature materials and their applications to power beaming," in *Proceedings of the 52nd IMPI's Microwave Power Symposium* (IMPI, Long Beach, CA, 2018), pp. 82–83.
[10]C. Hogan, B. Hoff, I. Rittersdorf, and V. Yakovlev, "Computational characterization of millimeter-wave heat exchangers with an AlN:Mo susceptor of multiple cylindrical elements," J. Microwav. Power Electromagnet. Energy **56**, 18–36 (2022).
[11]K. Parkin and T. Lambot, "Microwave thermal propulsion," Tech. Rep. (NASA, 2017), NASA/TP-2017-219555.
[12]S. Rostami, N. Ahmadi, and S. Khorasani, "Experimental investigations of thermo-exergitic behavior of a four-start helically corrugated heat exchanger with air/water two-phase flow," Int. J. Thermal Sci. **145**, 106030 (2019).
[13]G. A. Kriegsmann, "Thermal runaway in microwave heated ceramics: A one-dimensional model," J. Appl. Phys. **71**, 1960–1966 (1992).
[14]J. A. Pelesko and G. A. Kriegsmann, "Microwave heating of ceramic laminates," J. Eng. Math. **32**, 1–18 (1997).
[15]B. S. Tilley and G. A. Kriegsmann, "Microwave-enhanced chemical vapor infiltration: A sharp interface model," J. Eng. Math. **41**, 33–54 (2001).
[16]G. A. Kriegsmann and B. S. Tilley, "Microwave heating of laminate panels," J. Eng. Math. **44**, 173–198 (2002).
[17]J. M. Gaone, B. S. Tilley, and V. V. Yakovlev, "Permittivity-based control of thermal runaway in a triple-layer laminate," in *IEEE MTT-S International Microwave Symposium Digest* (IEEE, Honolulu, HI, 2017), pp. 459–462.
[18]J. M. Gaone, B. S. Tilley, and V. V. Yakovlev, "Electromagnetic heating control via high-frequency resonance of a triple-layer laminate," J. Eng. Math. **114**, 65–86 (2019).
[19]A. A. Mohekar, J. M. Gaone, B. S. Tilley, and V. V. Yakovlev, "A 2D coupled electromagnetic, thermal and fluid flow model: Application to layered microwave heat exchangers," in *IEEE/MTT-S International Microwave Symposium-IMS* (IEEE, 2018), pp. 1389–1392.
[20]A. A. Mohekar, B. S. Tilley, and V. V. Yakovlev, "A triple-layer electromagnetic heat exchanger with plane poiseuille flow: Control and local onset of thermal runaway," IEEE J. Multiscale Multiphys. Comput. Techniques **5**, 119–131 (2020).
[21]A. A. Mohekar, B. S. Tilley, and V. V.Yakovlev, "Plane wave irradiation of a layered system: resonance-based control over thermal runaway," in *17th International Conference on Microwave and High Frequency Heating (AMPERE 2019)* (Editorial Universitat Politècnica de València, 2019), pp. 292–300.
[22]J. Bear, *Dynamics of Fluids in Porous Media* (Courier Corporation, 2013).
[23]H. Ockendon and J. R. Ockendon, *Waves and Compressible Flow* (Springer, 2004).
[24]J. M. Hill and M. J. Jennings, "Formulation of model equations for heating by microwave radiation," Appl. Math. Modell. **17**, 369–379 (1993).
[25]D. J. Griffiths, *Introduction to Electrodynamics* (American Association of Physics Teachers, 2005).
[26]T. L. Bergman, F. P. Incropera, D. P. DeWitt, and A. S. Lavine, *Fundamentals of Heat and Mass Transfer* (John Wiley & Sons, 2011).
[27]V. V. Yakovlev, S. M. Allan, M. L. Fall, and H. S. Shulman, "Computational study of thermal runaway in microwave processing of zirconia," in *Microwave and RF Power Applications*, Cépaduès Éditions, edited by J. Tao (AMPERE, 2011), pp. 303–306.
[28]M. V. Dyke, *Perturbation Methods in Fluid Dynamics* (The Parabolic Press, 1978).
[29]V. Babu, *Fundamentals of Gas Dynamics*, 2nd ed. (Springer Cham, 2021).

[30]K. Brenan, S. Campbell, and L. Petzold, *Numerical Solution of Initial-Value Problems in Differential-Algebraic Equations* (SIAM, Philadelphia, PA, 1996).
[31]L. Shampine, M. Reichelt, and J. Kierzenka, "Solving index-1 DAEs in MATLAB and simulink," SIAM Rev. **41**, 538–552 (1999).
[32]L. Shampine, S. Thompson, J. Kierzenka, and G. Byrne, "Non-negative solutions of ODEs," Appl. Math. Comp. **170**, 556–569 (2005).
[33]R. D. Zucker and O. Biblarz, *Fundamentals of Gas Dynamics* (John Wiley & Sons, 2019).